

## Ultra Capacitor Based Sensorless Current Control of Grid Connected Inverter for Power Quality Improvement

<sup>1</sup> M.Ramya Kiranmayee (M.E), <sup>2</sup> B.Mothi Ram (M.E)

<sup>1</sup> Post Graduate Student (Power systems and Automation) SRKR Engineering College

<sup>2</sup> Assi.Professor SRKR Engineering Colleges

---

**Abstract-** The economical and environmental impacts of fossil fuels have forced governments and society to investigate sustainable solutions. The interest has focused principally on the green and clean benefits provided by renewable energy sources. The growth rate of new renewable energy supplies being installed has reached the incredible yearly mark of approximately 30% over the last few years. Consequently, investments in research and development in the field of power electronics have increased proportionally, especially in high voltage and high power grid connected systems. This paper presents ultra capacitor based sensorless current control of a three-phase inverter-based distributed generation system. a robust control scheme for high power quality grid connection of inductor–capacitor–inductor (LCL)-filtered distributed generation (DG) inverters. This paper also presents a modified adaptive Kalman filter for sensorless current control of a three-phase inverter-based distributed generation system. The control variable states can be estimated one sample in advance with a reduced number of sensors. Two current control loops with the steepest descent adaptive control for grid voltage estimation have been employed to boost robustness. Stability and dynamic performance have been examined. Simulation and results validate the proposed control approach. Simulation is done using Matlab software.

**Index Terms-** Distributed Generation (DG) Inverter, Inductor-capacitor-inductor (LCL) filter, Ultra capacitor (UC), Robust synchronization and control, Three- phase inverter Sensor less control, sensorless control.

---

### I. Introduction

RECENTLY, the development of renewable energy technologies have been accelerating, making the simultaneous development of power conversion devices for applications, such as wind and solar power systems extremely important but the majority of DG resources are interfaced to the utility grid or to the customer load via dc–ac pulse width modulated (PWM) current-controlled voltage source inverter (VSI) systems. Current-controlled VSIs are widely used in grid-connected applications due to the inherent converter-current protection, fast dynamic response, highly decoupled power flow control, and high power quality injection (with appropriate control strategy) to realize a cleaner and more efficient, reliable, resilient, and responsive power grids, the energy sector is moving into the era of smart grids (SGs) [1]–[4]. A major objective in future SGs is to maximize the penetration of distributed generation (DG) microgrids [5]–[8] in a way that enhances the overall grid stability, reliability and efficiency. UC characteristics and then goes on to provide a detailed comparison of various proposed control strategies to deduct the harmonics.

The demand for three-phase pulse width modulation (PWM) inverters in applications such as power control or grid connecting has been on the increase in recent years. Such inverters are connected to the grid via an  $L$  filter or an  $LCL$  filter to reduce the harmonics caused by the switching. An  $LCL$  filter can reduce the harmonics induced by low switching frequency and generates a satisfactory level of grid-side current. The grid-connection design guidelines for grid-connected VSIs with inductor–capacitor ( $LC$ ) filters are presented in [10]. Currently, there is a growing interest in using an inductor–capacitor–inductor ( $LCL$ ) ac-side filter in a grid-connected inverter, which yields better attenuation of switching harmonics, allows the use of a lower switching frequency that meets the harmonic limits, and reduces the electromagnetic interference. Accordingly, an  $LCL$ -filtered inverter is suitable for high power DG applications. The power generated by the synchronous generator is connected to the grid through the rectifier, inverter, and an  $LCL$  filter. However, the  $LCL$  filter complicates the dynamics of the DG interface system, particularly when the uncertain nature of the grid background distortion and system parameters is considered. The control requirements and associated difficulties can be pointed as follows.

1) The current controller should provide effective damping of grid-converter resonance with robustness against grid conditions and system parameters. However, depending on the grid configuration, a large set of grid impedance values is yielded as DG is commonly installed in weak grids with long radial distribution feeders [11], [12]. Furthermore, in the context of SG solutions, grid reconfiguration for self-healing and grid performance optimization remarkably affects the grid parameters at the point of common coupling (PCC) [2]. In

addition, cable overload, saturation, and temperature effects are all reasons for possible variation in the interfacing impedance seen by the inverter. Therefore, robust active damping of grid-converter resonance is essential.

2) High disturbance rejection of low-order grid distortion and unbalance [13]–[16]. Investigations in [13] showed that small distortion in the grid voltage remarkably increases the total harmonic distortion (THD) in the injected current and eventually, inverter instability can be reached due to possible interaction between grid distortion and DG interface. Under possible parameter variation, the bandwidth of harmonic resonance and dynamic interactions is remarkably expanded. Therefore, robust suppression of grid disturbances is one of the important properties that should be found in the current controller of an inverter-based DG unit.

3) High bandwidth current control performance. This feature is essential to maximize the disturbance rejection performance of low-order harmonics. Further, it allows accurate current tracking, facilitates current profiling for fast grid voltage regulation, and enhances the stability of the overall DG interface by minimizing the coupling among control loops. The digital control problems of grid-connected converter with *LCL* filters become more challenging when the ratio of the sampling and resonance frequencies is relatively low.

Different control schemes are proposed for *LCL*-filtered grid connected converters [17]–[23]. Major control techniques include proportional–integral (PI) control [20], resonant controllers [11], [12], and predictive/deadbeat control [19]. From the point of view of robustness against grid disturbances, the compensation capability of the low-order harmonics in the case of PI controllers—either in the stationary or in the synchronous reference frames—is very poor, yielding a major drawback when they are used in grid-connected and micro grid systems. Harmonic resonant controllers, tuned for selective harmonics elimination, can relax this problem. However, these controllers are tuned at preset frequencies and the stability is not verifiably guaranteed for large band of harmonic cancellations. These drawbacks are obvious in [13], which proposes a stationary frame resonant controller for grid-side current regulation. Similar problems can be traced in [15], where resonant synchronous frame controllers are emerged in the current control structure to mitigate the effect of grid harmonics. An additional drawback of using resonant controllers, either in the stationary or the synchronous reference frame, is the interaction with variation in grid impedance. Instability is yielded when the grid impedance shifts the bandwidth of the current controller to be lower than any of the resonant frequencies [12]. Due to their high bandwidth characteristics, deadbeat and predictive current controllers maximize the dynamic performance of the converter. However, the nature of these controllers as highly dependent model-based controllers increases the sensitivity against parameter variation and grid disturbances. It has been shown recently that deadbeat controllers are best-tailored for DG application if they are designed with enough robustness against parameter variation and system disturbances [20]. A hybrid PI and deadbeat controller is proposed in [21]. However, the robustness of the control system is not guaranteed due to the model-based nature of the proposed controller. To improve the harmonic distortion rejection performance, a robust repetitive feedback control of three-phase grid-connected VSIs with *LCL* filter is proposed in [22]. However, not all voltage disturbances are periodic by nature. Moreover, the repetitive control is not easy to stabilize for all unknown disturbances and cannot attain very fast response. Actually the DG sources are not giving continuous process because depends upon the nature. So, to reduce these distortions to implement the current at grid connection with the device of ultracapacitor Another constraint imposed on the tracking controller in *LCL*-filtered converters is the interaction between the active damping and tracking controllers.

This paper presents a robust line-voltage sensorless control scheme for *LCL*-filtered DG inverters. The proposed scheme addresses the aforementioned difficulties by providing: 1) robust and simple active damping control performance under grid and filter parameter variation; 2) suppression of grid-induced distortion without *a-priori* knowledge of the grid background distortion and unbalance; 3) robust deadbeat digital control performance that maximizes the dynamic performance of the converter; and 4) robustness against interaction dynamics between active damping and current tracking controllers. First, a simple and robust active damping controller is realized by drooping the inverter control voltage with the capacitor current. Second, the dynamics of the damping controller are augmented with the plant dynamics to design an augmented deadbeat current controller. The latter is designed with a delay compensation method that forces the delays elements which are caused by voltage calculation, PWM, and synchronous frame rotation to be equivalently placed outside the close-loop control system. Hence, their effect on the closed-loop stability is eliminated and the current controller can be designed with high bandwidth characteristics to facilitate fast current tracking and higher bandwidth for disturbance rejection. Third, to provide internal model dynamics within the current control loop against grid harmonics, unbalance, and disturbances generated by parameter variation, an adaptive estimator is emerged in the control structure to construct the internal model in real time and in adaptive nature (as opposed to resonant controllers, which are tuned are preset modes). The estimated internal model dynamics are used to realize a control system for the DG interface featuring line-voltage sensorless current and synchronization performance, which enhances the reliability and cost measures of the DG interface. Theoretical analysis and comparative evaluation results are presented to demonstrate the effectiveness of the proposed control scheme.

## II. Three-Phase Current-Controlled Grid-Connected Vsi With Lcl Filter

### A. Basic System Equations

A system topology of a grid-connected current-controlled VSI with a  $T$ -type  $LCL$  filter is depicted in Fig. 1, here  $R_1$  and  $L_1$  represent the resistance and inductance of the inverter side filter inductor;  $R_2$  and  $L_2$  represent the equivalent resistance and inductance of the grid-side filter inductor and grid;  $C_f$  is the filter capacitance;  $v_s$  is the grid voltage;  $v_c$  is the filter capacitor voltage;  $i_g$  is the injected grid current;  $i_{inv}$  is the inverter output current; and  $v_{inv}$  is the inverter output voltage. Using the voltage-oriented control principle, the active and reactive power injection can be controlled via high-level controller that generates the current references.

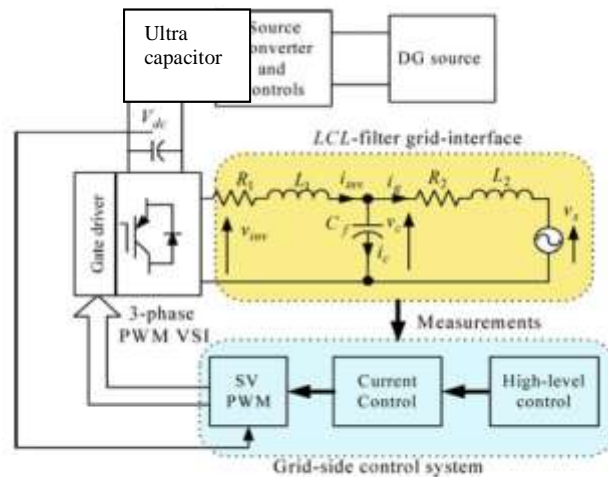


Fig. 1. Grid-connected three-phase VSI with an inner current control loop and  $T$ -type  $LCL$  filter.

In the natural reference frame, the per-phase power-circuit dynamics can be represented by the following model:

$$\left. \begin{aligned} L_1 \frac{di_{inv}}{dt} &= v_{inv} - v_c - R_1 i_{inv} \\ L_2 \frac{di_g}{dt} &= v_c - v_s - R_2 i_g \\ C_f \frac{dv_c}{dt} &= i_{inv} - i_g \end{aligned} \right\} \quad (1)$$

In Park's  $d-q$  frame that rotates synchronously with the grid angular speed, the injected active and reactive power components  $p$  and  $q$ , respectively, can be represented in terms of the  $d$ - and  $q$ -axes components of the supply voltage at the PCC and the injected currents as follows:

$$p = \frac{3}{2} (v_{ds} i_{dg} + v_{qs} i_{qg}) \quad (2)$$

$$q = \frac{3}{2} (v_{qs} i_{dg} - v_{ds} i_{qg}) \quad (3)$$

Where  $v_{ds}$ ,  $v_{sq}$  and  $i_{dg}$ ,  $i_{qg}$  are the  $d$ - and  $q$ -axes components of the supply voltage at the PCC, and the grid-side current, respectively. In addition, the magnitude of the voltage at the PCC is given by

$$|v_s| = \sqrt{v_{sd}^2 + v_{sq}^2} \quad (4)$$

Considering the physical constraints, the preceding model is subjected to the following limits. The injected current is limited to the maximum continuous current of the inverter or to the maximum available current of the inverter in a limited short time operation. Also, the load voltage is limited to the maximum available output voltage of the inverter depending on the dc-link voltage.

B. Converter Resonance Damping

Converter resonance damping is essential to maintain converter stability, facilitate high bandwidth current control, and facilitate effective mitigation of grid-induced distortion in the output current. A simple and robust technique to damp LC filter resonance can be achieved by injecting a damping voltage that is proportional to the capacitor current in the power circuit [23]. This method can be extended to the case of LCL filters. Accordingly, the dynamics of the actively damped system can be given by

$$\left. \begin{aligned} L_1 \frac{di_{inv}}{dt} &= v_{inv} - v_d - v_c - R_1 i_{inv} \\ v_d &= R_d (i_{inv} - i_g) \\ L_2 \frac{di_g}{dt} &= v_c - v_s - R_2 i_g \\ C_f \frac{dv_c}{dt} &= i_{inv} - i_g \end{aligned} \right\} \quad (5)$$

Where  $v_d$  is the injected damping voltage, and  $R_d$  is the damping coefficient of the LCL filters.

The fact that the damping voltage does not depend on the resonance frequency yields a robust damping performance. Further, the fact that the capacitor current is inherently small yields a small bounded damping voltage that does not remarkably affect the voltage capability of the inverter. Further, a low-pass filtered capacitor current can be used to reject high-frequency noise components and maintain the power quality indices of the injected line currents.

To analyze the system performance with active damping control, the open-loop current dynamics with active damping is given by, (6) as shown at the bottom of this page, whereas the closed-loop dynamics with a PI controller is given by, (7) as shown at the bottom of this page, where  $K_p$  and  $K_I$  are the Proportional and integral gains of the PI controller, and the superscript “\*” denotes the reference value.

$$I_g(s) = \frac{1}{L_1 L_2 C_f s^3 + C_f (L_1 R_2 + L_2 R_1 + L_2 R_d) s^2 + (R_1 R_2 C_f + R_d R_2 C_f L_1 + L_2) s + (R_1 + R_2)} V_{inv}(s) \quad (6)$$

$$\frac{L_1 C_f s^2 + C_f (R_1 + R_d) s + 1}{L_1 L_2 C_f s^3 + C_f (L_1 R_2 + L_2 R_1 + L_2 R_d) s^2 + (R_1 R_2 C_f + R_d R_2 C_f L_1 + L_2) s + (R_1 + R_2)} V_s(s)$$

$$I_g(s) = \frac{K_p s + K_I}{L_1 L_2 C_f s^4 + C_f (L_1 R_2 + L_2 R_1 + L_2 R_d) s^3 + (R_1 R_2 C_f + R_d R_2 C_f + L_1 + L_2) s^2 + (R_1 + R_2 + K_p) s + K_I} I_g^*(s)$$

$$- \frac{L_1 C_f s^3 + C_f (R_1 + R_d) s^2 + s}{L_1 L_2 C_f s^4 + C_f (L_1 R_2 + L_2 R_1 + L_2 R_d) s^3 + (R_1 R_2 C_f + R_d R_2 C_f + L_1 + L_2) s^2 + (R_1 + R_2 + K_p) s + K_I} V_s(s) \quad (7)$$

With grid-side current feedback control, the harmonic impedance of the converter is given by, (8) as shown at the bottom of this page. Similarly, with converter-side current feedback control, the harmonic impedance of the converter is given by, (9) as shown at the bottom of this page. Fig. 2 shows the frequency characteristics of a 200-kW converter with 5-kHz switching frequency and the LCL filter with active damping control. Fig. 2(a) shows the open-loop frequency characteristics with different values of  $R_d$ . The resonance peak can be completely damped, and accordingly, larger control bandwidth can be obtained. Fig. 2(b) shows the open-loop frequency characteristics with  $R_d = 8 \Omega$  and uncertain grid conditions. Robust active damping performance can be achieved without strict information on system parameters. Fig. 2(c) shows the harmonic impedance in both cases of  $i_g$  feedback and  $i_{inv}$  feedback control. The parallel resonant mode is effectively damped in both schemes. However, the harmonic impedance might not be high enough to reject low-order harmonics and grid voltage disturbances. Therefore, the current controller should provide effective disturbance rejection against harmonic, unbalanced and random voltage disturbances, which are characterized by unknown frequency content. The proposed deadbeat current controller with adaptive internal model dynamics is designed to meet these requirements. To enhance the disturbance rejection performance, proportional harmonic resonant controllers (P-HRES) can be applied to provide internal model dynamics at selected harmonic frequencies.

$$G_{P-HRES}(s) = k_p + \sum_{h=1}^n \frac{k_{hs}}{s^2 + (h\omega_c)^2} \quad (10)$$

The transfer function of the P-HRES is defined as where  $K_p$  is the proportional gain,  $h$  is the harmonic order,  $k_i h$  is the resonant filter gain at harmonics  $h$ ,  $n$  is the upper limit of harmonic order,  $\omega_o$  is the fundamental angular frequency, and  $s$  is the complex frequency. The proportional resonant controller can reduce the effect of the grid-induced harmonics in the injected currents; however, the stability is not verifiably guaranteed under interfacing parameter variation. Instability occurs once when one or more of the resonant frequencies lie outside the loop bandwidth.

### III. Current Control Design

#### A. Augmented Discrete-Time State-Space Model

To account for the active damping dynamics, external disturbances, possible uncertainties in system parameters, and system delays, an augmented discrete-time state-space model is developed. Since both the converter and distribution system parameters are uncertain and dynamic in nature due to factors such as grid parameter variation, cable overload, transformer saturation, and temperature effects, the uncertainty in system parameters should be considered in control system design. Using the nominal system parameters and considering the grid-voltage as a dynamic disturbance, the system dynamics in (5) can be rewritten as follows:

$$Z(s)_H \equiv \left. \frac{V_g(s)}{I_g(s)} \right|_{I_a(s)}$$

$$= \frac{L_1 L_2 C_f s^4 + C_f (L_1 R_2 + L_2 R_1 + L_2 R_d) s^3 + (R_1 R_2 C_f + R_d R_2 C_f + L_1 + L_2) s^2 + (R_1 + R_2 + K_p) s + K_I}{L_1 C_f s^3 + C_f (R_1 + R_d) s + 1} \quad (8)$$

$$Z(s)_H \equiv \left. \frac{V_g(s)}{I_g(s)} \right|_{I_{inv}(s)}$$

$$= \frac{L_1 L_2 C_f s^4 + C_f (L_1 R_2 + L_2 R_1 + L_2 R_d + L_2 K_p) s^3 + (C_f (R_1 R_2 + R_d R_2 + R_2 K_p + K_I L_2) + L_1 + L_2) s^2 + (R_1 + R_2 + K_p + R_2 C_f K_I) s + K_I}{L_1 C_f s^3 + (C_f (R_1 + R_d) + K_p) s + (1 + C_f K_I) s} \quad (9)$$

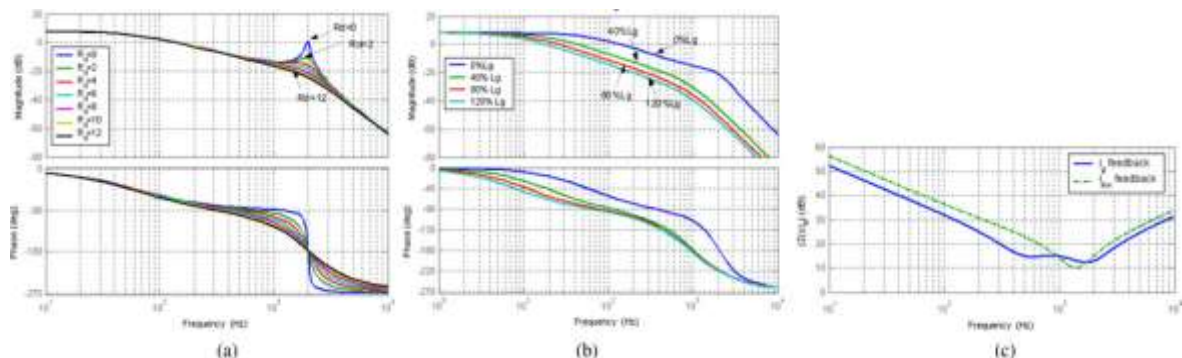


Fig. 2. Frequency characteristics of the actively-damped system. (a) Open-loop frequency response at different values of  $R_d$ . (b) Open-loop frequency response with  $R_d = 8 \Omega$  and variable grid inductance. (c) Harmonic impedance with converter-side and grid-side current feedback control.

Where the subscript “o” denotes the nominal value, and  $W(t)$  Represents the lump of uncertainties caused by parameter

$$y(t) = Cx(t)$$

$$x = \begin{bmatrix} i_{inv} \\ i_g \\ v_c \end{bmatrix} \quad A_o = \begin{bmatrix} -\frac{(R_{1o} + R_d)}{L_{1o}} & \frac{R_d}{L_{1o}} & -\frac{1}{L_{1o}} \\ 0 & -\frac{R_{2o}}{L_{2o}} & -\frac{1}{L_{2o}} \\ \frac{1}{C_{fo}} & -\frac{1}{C_{fo}} & 0 \end{bmatrix}$$

$$G_o = \begin{bmatrix} -\frac{1}{L_{1o}} & 0 & 0 \\ 0 & -\frac{1}{L_{2o}} & 0 \\ 0 & 0 & -\frac{1}{C_{fo}} \end{bmatrix} \quad B_o = \begin{bmatrix} \frac{1}{L_{1o}} & 0 & 0 \end{bmatrix}^T$$

$$C = [1 \quad 0 \quad 0] \quad (11)$$

Uncertainties; and it is given by

$$W(t) = \begin{bmatrix} w_1(t) \\ w_2(t) \\ w_3(t) \end{bmatrix} = \begin{bmatrix} \Delta R_1 i_{inv} + \Delta L_1 \frac{di_{inv}}{dt} + n_1 \\ \Delta R_2 i_g + \Delta L_2 \frac{di_g}{dt} + v_d + n_2 \\ \Delta C_f \frac{dv_c}{dt} + n_3 \end{bmatrix} \quad (12)$$

Where the symbol “Δ” denotes the deviation from nominal values, and  $n_1$ ,  $n_2$ , and  $n_3$  represent unstructured uncertainties due to unmodeled dynamics. Provided that the harmonic components included in the inverter output voltage are not correlated with the sampled reference currents and with symmetrical PWM, the PWM VSI can be assumed as a zero-order hold circuit with a sampling time  $T_s$ . For digital implementation of the control algorithm, the plant dynamics can be represented in discrete time as follows:

$$A_{do} = e^{A_o T_s} \approx \begin{bmatrix} 1 - \frac{T_s(R_{1o} + R_d)}{L_{1o}} & \frac{T_s R_d}{L_{1o}} & -\frac{T_s}{L_{1o}} \\ 0 & 1 - \frac{T_s R_{2o}}{L_{2o}} & \frac{T_s}{L_{2o}} \\ \frac{T_s}{C_{fo}} & -\frac{T_s}{C_{fo}} & 1 \end{bmatrix}$$

$$B_d = \int_0^{T_s} e^{A_o(T_s-\tau)} B_o d\tau \approx \begin{bmatrix} \frac{T_s}{L_{1o}} & 0 & 0 \end{bmatrix}^T$$

$$G_d = \int_0^{T_s} e^{A_o(T-\tau)} G_o d\tau \approx \begin{bmatrix} -\frac{T_s}{L_{1o}} & 0 & 0 \\ 0 & -\frac{T_s}{L_{2o}} & 0 \\ 0 & 0 & -\frac{T_s}{C_{fo}} \end{bmatrix}$$

To account for the computational time-delay associated with the digital implementation, one-sample delay exists between the control voltage  $u_{inv}(k)$  and the inverter’s terminal voltage, i.e.,  $v_{inv}(k+1) = u_{inv}(k)$ . Accordingly, (13) can be extended to account for this time delay as follows:

$$X(k+1) = A_{do}x(k) + B_{do}v_{inv}(k-1) + G_{do}W(k)$$

$$y(k) = Cx(k) \quad (14)$$

The model in (14) represents the augmented uncertain power Circuit dynamics and facilitates robust control design.

### B. Deadbeat Current Control

In order to enhance the bandwidth characteristics, in the presence of system delays, a delay compensation method is proposed in this paper. The compensation method adopts a natural observer and utilizes the predictive nature of the outputs of the internal model generator (described in Section IV-C) to force the delay element to be equivalently placed outside the closed-loop control system. Hence, its effect on the closed-loop stability is eliminated and the current controller can be designed with high bandwidth characteristics. Further, system uncertainties are inherently included in the delay compensation method, which yields robust overall control performance. During the  $(k+1)$ th period of the control process, the current is forced by the control voltage at  $(k+1)$  which is calculated in the  $k$ th period. The resultant current, which is sensed at the beginning of the  $(k+2)$ th period, can be given by

$$i_{inv}(k+2) = \left(1 - \frac{T_s(R_{1o}+R_d)}{L_{1o}}\right) i_{inv}(k+1) + \left(\frac{T_s R_d}{L_{1o}}\right) i_{inv}(k+1) - \frac{T_s}{L_{1o}} (v_c(k+1) - u(k) + w_1(k+1)) \quad (15)$$

The grid-side current at  $(k+2)$  is affected by control voltage at  $(k)$ ; i.e., a two-sample delay system. Using (14),  $i_{inv}(k+1)$ ,  $i_g(k+1)$ , and  $v_c(k+1)$  can be obtained and substituted in (15), to obtain the converter-side current at  $(k+2)$  as follows:

$$i_{inv}(k+2) = K_1 x(k) + K_2 W(k) + K_3 u(k-1) + K_4 (u(k) - w_1(k+1)) \quad (16)$$

Where

$$K_1 = \begin{bmatrix} \left(1 - \frac{T_s(R_{1o}+R_d)}{L_{1o}}\right)^2 - \frac{T_s^2}{L_{1o}C_{fo}} \\ \frac{2T_s R_d}{L_{1o}} - \frac{T_s^2 R_d (R_{1o}+R_d)}{L_{o1}^2} - \frac{T_s^2 R_d R_{2o}}{L_{1o}L_{2o}} + \frac{T_s^2}{L_{1o}C_{fo}} \\ \frac{T_s^2 R_d (R_{1o}+R_d)}{L_{o1}^2} - \frac{2T_s}{L_{1o}} + \frac{T_s^2 R_d}{L_{1o}L_{2o}} \end{bmatrix}^T$$

$$K_2 = \begin{bmatrix} \frac{T_s^2(R_{1o}+R_d)}{L_{1o}^2} - \frac{T_s}{L_{1o}} \\ -\frac{T_s^2 R_d}{L_{1o}L_{2o}} \\ \frac{T_s^2}{L_{1o}C_{fo}} \end{bmatrix}^T$$

$$K_3 = \frac{T_s}{L_{1o}} - \frac{T_s^2(R_{1o}+R_d)}{L_{1o}^2}$$

$$K_4 = \frac{T_s}{L_{1o}}$$

For current regulation,  $i_{inv}(k+2)$  can be regarded as the reference. Accordingly, the appropriate control voltage can be predictably obtained as follows:

$$u^*(k) = \frac{1}{K_4} \{i_{inv}^*(k+2) - K_1 x(k) - K_2 W(k) - K_3 u(k-1) - i_{inv}^*(k)\} + w_1(k+1) \quad (17)$$

Where the subscript “\*” denotes the reference value. The control voltage can be calculated using the measured and estimated quantities  $W(k)$  and  $w_1(k+1)$ . Therefore, the delay is equivalently removed outside the closed-loop control to appear in the two-step ahead reference vector. Under the assumption of known internal model dynamics  $W$ , and by using (17), the output current can be given as

$$i_{inv}(k) = i_{inv}^*(k-2) \quad (18)$$

Accordingly, the frequency response of the reference-to output Transfer function is

$$s G(e^{j\omega T_s}) = e^{-2j\omega T_s} \quad (19)$$

Which has a unity gain and a phase lag corresponds to the two sampling- period delay, which are equivalently removed outside the closed loop to appear in the reference side. To compensate for this delay, the forward estimate of the reference current is necessary. This equivalently works as adding an equal and opposite phase shift to the reference trajectory. Based on real-time analysis, a two-step forward prediction provides the necessary phase advance to minimize the steady-state error. As a result, the reference current is predicted as follows:

$$i_{inv}^*(k+2) = 3i_{inv}^*(k) - 2i_{inv}^*(k-1) \quad (20)$$

The utilization of the estimated internal model dynamics provides efficient means for control effort energy shaping and provides the necessary phase advance of the estimated disturbance, which compensates for the total system's delay.

*C. Robust Line-Voltage Sensorless Current Control*

To ensure high disturbance rejection of grid distortion and parametric instabilities, an adaptive estimator for unknown dynamics  $W$  is proposed and emerged in the deadbeat control structure. The proposed real-time internal model generator extends the idea of using harmonic resonant modes in the current control loop to enhance the harmonic disturbance rejection by providing internal model dynamics that are adaptive in nature. The direct result of the proposed approach is shaping the harmonic impedance of the converter adaptively to reject unknown harmonic distortion and voltage disturbances associated with parameter variation. The fast response of the deadbeat controller makes it applicable to any reference frame. Therefore, it can be applied to the natural or the stationary  $\alpha\beta$ -frame, where the effect of grid-voltage unbalance can be inherently rejected. Further, the fact that the grid voltage disturbance is embedded in the unknown internal model dynamics facilitates the realization of a line-voltage-sensorless current control scheme. Voltage sensorless control enhances the robustness of the control performance by eliminating the residual negative sequence and voltage feed-forward compensation errors. Further, with reliable estimation of the grid voltage, a voltage-sensorless phase-locked loop (PLL) can be realized. With voltage sensorless current control and synchronization, system reliability and cost can be improved by reducing the number of feedback signals to the controller. Based on the augmented model, a simple adaptive observer with the following I/O relation can be constructed:

$$\hat{x}(k+1) = A_{do}\hat{x}(k) + B_{do}u_{inv}(k-1) + G_{do}\hat{W}(k) \tag{21}$$

Where  $\hat{x}$  is the output of the adaptive observer, and  $\hat{W}$  is the Estimated internal model dynamics. The convergence of the proposed observer can be achieved with an appropriate disturbance adaptation using the estimation error

$$e(k) = x(k) - \hat{x}(k)$$

A discrete-type quadratic error function is defined as follows:

$$E(k) = \frac{1}{2} e(k)^T e(k) \tag{22}$$

The disturbance voltage can be adaptively estimated by minimizing the error function  $E(k)$  by performing the steepest descent method on a surface in  $\hat{W}$  space where its height is equal to the measured error [24]. In order to minimize the error function  $E(k)$ , one can evaluate the following Jacobian:

$$J = \frac{\partial E}{\partial \hat{W}} = \frac{\partial E}{\partial e} \frac{\partial e}{\partial x} \frac{\partial x}{\partial \hat{W}} = -G_{do}e \tag{23}$$

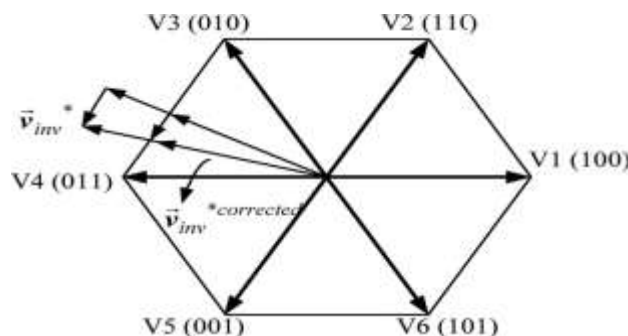


Fig. 3. Control voltage limit in the space vector plane.

For the steepest descent algorithm, the change in the weight is calculated as

$$\begin{aligned} \hat{W}(k+1) &= \hat{W}(k) + \Delta\hat{W}(k) = \hat{W}(k) - MJ \\ &= \hat{W}(k) + MG_{do}e \end{aligned} \tag{24}$$

$$M = \begin{bmatrix} m_1 & 0 & 0 \\ 0 & m_2 & 0 \\ 0 & 0 & m_3 \end{bmatrix}$$

is an adaptation gain matrix.

Therefore, the estimated internal model dynamics can be used to robustly calculate the control voltage as follows:

$$u^*(k) = \frac{1}{K_4} \{i_{inv}^*(k+2) - K_1 x(k) - K_2 \hat{W}(k) - K_3 u(k-1)\} + \hat{w}(k+1) \quad (25)$$

The control law in (25) can be easily tuned using nominal system parameters and it can be synthesized using a PWM technique. The control algorithm is implemented in the stationary  $\alpha\beta$  reference frame to reduce the computational demand. Since the reference current vector is generated in the synchronous reference frame, the effect of the synchronous frame rotation should be considered to minimize the phase lag in the injected current. Since the control voltage is applied during the  $(k+1)$ th period, the position difference can be adjusted by averaging the reference frame position over one switching period. Therefore, the corrected voltage command can be given in the following space vector form:

$$\hat{v}_{inv}^*(k+1) = v_{inv}^*(k+1) e^{j(2.5\theta(k) - 1.5\theta(k-1))} \quad (26)$$

Where  $\theta(k)$  is the synchronous frame position at the current sampling period. To achieve higher dc-link voltage utilization and lower distortion in the output current, the space-vector modulation (SVM) technique can be employed to synthesize the control voltage in (27). The control voltage limit method utilizes the space vector voltage limit in the same direction of the reference voltage as shown in Fig. 3.

#### D. Convergence Analysis

As a two-degree-of-freedom (2-DOF) predictive control system, the stability of the internal model controller and predictive controller can be analyzed independently [25].

First, this section analyzes the stability of the internal model

Controller and provides a guideline in tuning the controller parameters in the sense of Lyapunov functions [24]. The Lyapunov function is selected as

$$V_T(e(k), k) = \frac{1}{2} e(k)^T e(k) \quad (27)$$

Lyapunov's convergence criterion must be satisfied such that

$$V_T(k) \Delta V_T(k) < 0 \quad (28)$$

Where  $\Delta V_T(k)$  is the change in the total Lyapunov function.

The change in the Lyapunov function is given by

$$\Delta V_T(k) = V_T(e(k+1)) - V_T(e(k)) < 0 \quad (29)$$

The change in the error  $\Delta e(k)$  due to the adaptation of the adaptive internal model generator can be given by

$$\begin{aligned} \Delta e(k) &= e(k+1) - e(k) = \frac{\partial e(k)}{\partial \hat{W}(k)} \Delta \hat{W}(k) \\ &= \frac{\partial e(k)}{\partial x(k)} \frac{\partial x(k)}{\partial \hat{W}(k)} \Delta \hat{W}(k) \\ &= -G_{do} M G_{do} e(k). \end{aligned} \quad (30)$$

Accordingly,  $\Delta V_T(k)$  can be represented as

$$\begin{aligned} \Delta V_T(k) &= e(k)^T \Delta e(k) + \frac{1}{2} \Delta e(k)^T \Delta e(k) \\ &= -e(k)^T \left[ G_{do} M G_{do} \left( I_{3 \times 3} - \frac{1}{2} G_{do} M G_{do} \right) \right] e(k). \end{aligned} \quad (31)$$

To satisfy the stability condition in (28), the adaptation gains are chosen as

$$0 < m_1 < \frac{2}{\max_k [\|\partial \hat{i}_{inv}(k) / \partial \hat{v}_1\|^2]} \text{ or } 0 < m_1 < \frac{2I_{dc}^2}{T^2} \quad (32)$$

$$0 < m_2 < \frac{2}{\max_k [\|\partial \hat{i}_g(k) / \partial \hat{v}_2\|^2]} \text{ or } 0 < m_2 < \frac{2I_{dc}^2}{T^2} \quad (33)$$

$$0 < m_3 < \frac{2}{\max_k [\|\partial \hat{v}_c(k) / \partial \hat{v}_3\|^2]} \text{ or } 0 < m_3 < \frac{2C_{fc}^2}{T^2} \quad (34)$$

Where  $\|\cdot\|$  is the Euclidean norm in  $\mathbb{R}^n$ .

Using the abovementioned condition, it can be seen that  $\Delta V_T(k) < 0$  and it follows that the adaptation error is monotonically nonincreasing. Therefore, the convergence is guaranteed,

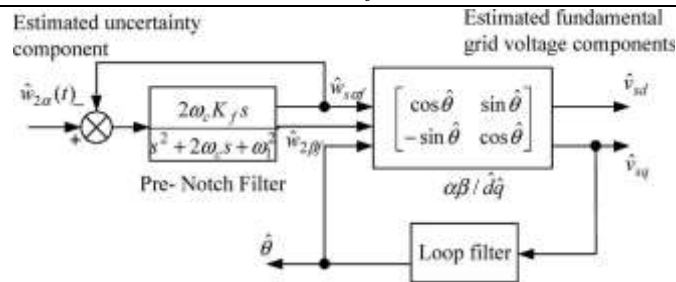


Fig. 4. Synchronization loop.

i. i.e.,  $\tilde{W}(k)$  and  $e(k) \rightarrow 0$  and as  $k \rightarrow \infty$ , where  $\tilde{W}(k) = W(k) - \hat{W}(k)$  is the internal model estimation error vector. *Second*, the stability and robustness of the predictive control scheme can be analyzed by considering the augmented discrete time current dynamics and the robust control law in (25) as follows:

$$\begin{aligned}
 i_{inv}^*(k+2) &= K_2 W(k) + i_{inv}^*(k+2) - K_2 \hat{W}(k) \\
 &\quad + K_4 \hat{w}_2(k+1) - K_4 w_2(k+1) \\
 &= i_{inv}^*(k+2) - K_2 \tilde{W}(k) + K_4 \tilde{w}_2(k+1) \quad (35)
 \end{aligned}$$

As seen in (36), the current tracking error is proportional to the uncertainty estimation error. According to preceding convergence analysis, the convergence of the observation and internal model generation is guaranteed. Therefore,

$$i_{inv}^*(k) - i_{inv}(k) \rightarrow 0 \text{ as } k \rightarrow \infty.$$

**E. Voltage-Sensorless Synchronization**

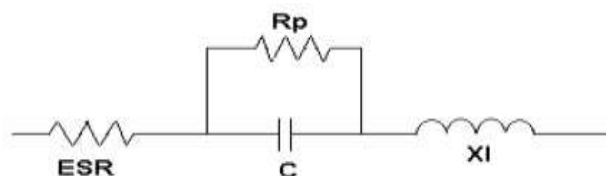
The uncertainty function  $w_2(t)$  contains the grid voltage information and other disturbances such as low- and high-order harmonics, which may have been produced by the power converter itself or propagated through the system, and grid voltage unbalance. The fact that converter synchronization is based on the fundamental grid voltage facilitates the use of the uncertainty function to extract the fundamental grid voltage vector without using voltage sensors. Toward this, a simple voltage sensorless synchronization method is adopted. The method utilizes a  $dq$ based PLL with a resonant prefilter tuned at the fundamental grid frequency, which is fairly constant to extract the fundamental component of the estimated uncertainty function. Accordingly, the fundamental component of the uncertainty function can  $w_2(t)$  be estimated and used for grid synchronization. Fig. 4 shows the synchronization loop structure. Fig. 5 shows the proposed interfacing scheme for a current controlled  $LCL$ -filtered PWM-VSI when applied to a renewable DG source, such as photovoltaic arrays and full-scale wind turbines. The scheme consists of the proposed deadbeat current controller, adaptive internal model generator and voltage sensorless synchronization loop.

**F. ULTRA CAPACITOR**

Electrochemical capacitors (ECs), variously referred to by manufacturers in promotional literature as Super capacitors also called ultra capacitors and electric double layer capacitors (EDLC) are capacitors with capacitance values greater than any other capacitor type available today. Capacitance values reaching up to 400 Farads in a single standard case size are available. The most significant advantage supercapacitors have over batteries is their ability to be charged and discharged continuously without degrading like batteries do. This is why batteries and supercapacitors are used in conjunction with each other. The supercapacitors will supply power to the system when there are surges or energy bursts since supercapacitors can be charged and discharged quickly while the batteries can supply the bulk energy since they can store and deliver larger amount energy over a longer slower period of time. Ultra capacitors construction different from other capacitors types are the electrodes used in these capacitors. Ultra capacitors are based on a carbon (nano tube) technology. This technology cans creat large surface area. Ultra capacitor is a double layer capacitor; the energy is stored by charge transfer at the boundary between electrode and electrolyte.

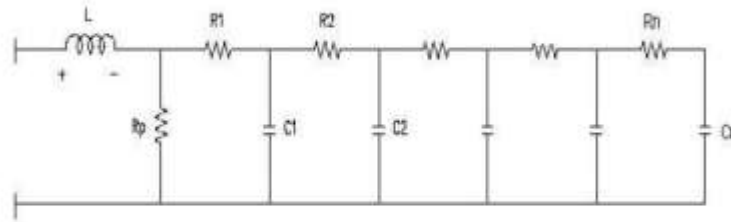
**Equivalent circuit**

Ultra capacitors can be illustrated similarly to conventional film, ceramic or aluminum electrolytic capacitors



## Ultra Capacitor Based Sensorless Current Control Of Grid Connected Inverter For Power Quality

In actuality Ultra capacitors exhibit a non ideal behavior due to the porous materials used to make the electrodes. This causes Ultra capacitors to exhibit behavior more closely to transmission lines than capacitors. Below is a more accurate illustration of the equivalent circuit for an Ultra Capacitor



Super capacitors are expensive in terms of cost per watt. Some design engineers argue that the money for the super capacitor would better be spent on a larger battery. The super capacitor can be charged and discharged virtually an unlimited number of times. Unlike the electrochemical battery, which has a defined cycle life, there is little wear and tear by cycling a super capacitor. Nor does age affect the device, as it would a battery. Under normal conditions, a super capacitor fades from the original 100 percent capacity to 80 percent in 10 years. Applying higher voltages than specified shortens the life. The super capacitor functions well at hot and cold temperatures.

The self-discharge of a super capacitor is substantially higher than that of an electrostatic capacitor and somewhat higher than the electrochemical battery. The organic electrolyte contributes to this. The stored energy of a super capacitor decreases from 100 to 50 percent in 30 to 40 days. A nickel-based battery self-discharges 10 to 15 percent per month. Li-ion discharges only five percent per month.

### Advantages and Disadvantages of Super capacitors:

#### Advantages:

- I. Virtually unlimited cycle life - not subject to the wear and aging experienced by the electrochemical battery.
- II. Low impedance - enhances pulse current handling by paralleling with an electrochemical battery.
- III. Rapid charging - low-impedance supercapacitors charge in seconds.
- IV. Simple charge methods - voltage-limiting circuit compensates for self-discharge; no full-charge detection circuit needed.
- V. Cost-effective energy storage - lower energy density is compensated by a very high cycle count.

#### Disadvantages:

- I. Unable to use the full energy spectrum - depending on the application, not all energy is available.
- II. Low energy density - typically holds one-fifth to one-tenth the energy of an electrochemical battery.
- III. Cells have low voltages - serial connections are needed to obtain higher voltages.
- IV. Voltage balancing is required if more than three capacitors are connected in series.
- V. High self-discharge - the self-discharge is considerably higher than that of an electrochemical battery.

## IV. Evaluation Results

To evaluate the performance of the proposed control scheme, a three-phase PWM-VSI system incorporated with the proposed control scheme, as reported in Fig. 5, has been implemented. The system parameters are as follows: grid phase voltage = 120V at 60 Hz, nominal parameters  $L_1 = 0.8$  mH,  $R_1 = 0.2$   $\Omega$ ,  $L_2 = 0.2$  mH +  $L_g$ ,  $R_2 = 0.2$   $\Omega$  +  $R_g$ ,  $L_g = 0-5.8$  mH,  $R_g = 0-0.5$   $\Omega$ , and  $C_f = 40$   $\mu$ F. The real-time code of the proposed control scheme is generated by the Real-Time Workshop, under MATLAB/Simulink environment. The TMS320F28335 digital signal processor has been chosen as an embedded platform for experimental validation with switching frequency of 8 kHz. The synchronous sampling technique with a symmetric SVM module is adopted. With this method, the sampling is performed at the beginning of each modulation cycle. Only two phases current are fed back as the neutral is isolated. To verify the feasibility of the proposed controller, different operating conditions have been considered. For the purpose of performance comparison, the proposed control scheme is compared to the following key current controllers in DG applications:

- 1) P-HRES controller [12].
- 2) Predictive controller [20].

The controllers under comparison are tested under the following grid distortion conditions: grid voltage harmonics: 3% 5th harmonic, 2% 7th harmonic, 1% 11th harmonic, 1% 13<sup>th</sup> harmonic, and 0.5% 17th harmonics; grid voltage unbalance: 7% voltage unbalance factor. In the ex

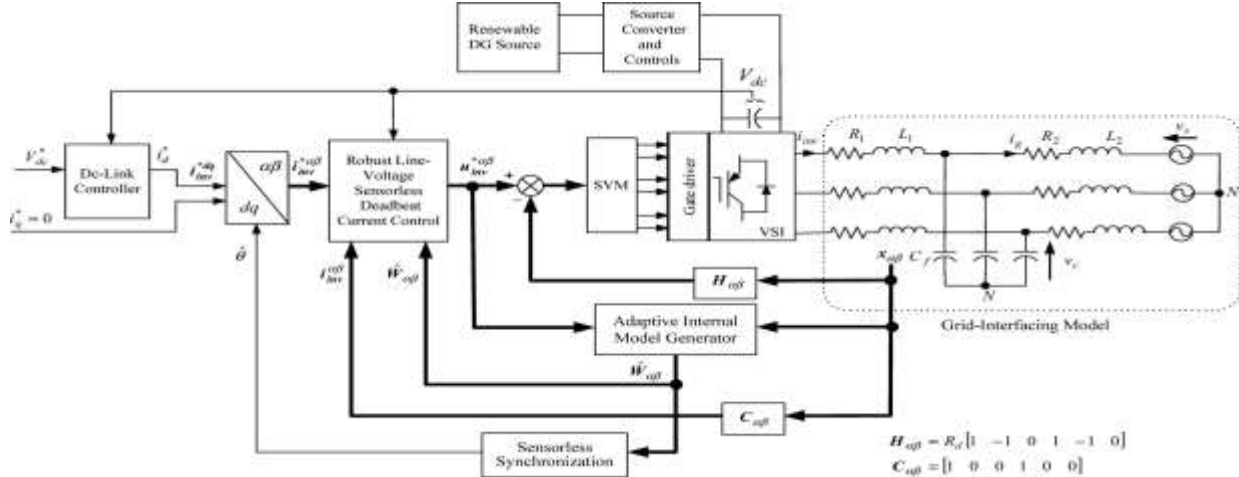


Fig. 5. Proposed control scheme.

Aimed controllers, the magnitude of the current command is set at 20A with unity power factor for  $t \geq 0$  s. Initially, the actual grid voltages are used only for synchronization. First, the performance of the P-HRES is evaluated. The controller provides internal model dynamics at selected harmonic frequencies. Fig. 6(a) shows the control performance of the P-HRES controller with harmonic compensators tuned at the fundamental, 5th, 7th, 11th, 13th, and 17th harmonics at nominal system parameters. The current quality is improved due to the presence of internal models that are tuned at the grid distortion modes. Fig. 6(b) shows the control performance of the P-HRES controller with harmonic compensators tuned at the fundamental, 5th, 7th, 11th, 13th, and 17th harmonics and 50% mismatch in the grid inductance. The mismatch in the grid inductance shifts the effective open-loop bandwidth of the P-HRES controller and leads to current control instability as shown in Fig. 6(b). Fig. 6(c) shows the frequency characteristics of the open loop P-HRES controller at nominal grid inductance and 35% grid inductance. In the latter case, the resonant mode of the 13th and 17th harmonics lies outside the reduced bandwidth leading to sustained oscillations in the output current. These oscillations and the poor dynamic response are indeed the result of the instability of the control system. The current control limits and overmodulation of the PWM limit the magnitude of these oscillations (limit cycles). Active damping control can mitigate such instability; however, the active damping controller should be tuned at a specified grid inductance or power circuit parameters in general. The effectiveness of the active damping control is lost even with small uncertainty in system parameters, which leads to a remarkable shift the resonance frequency of the power circuit [11]. Second, the performance of the predictive

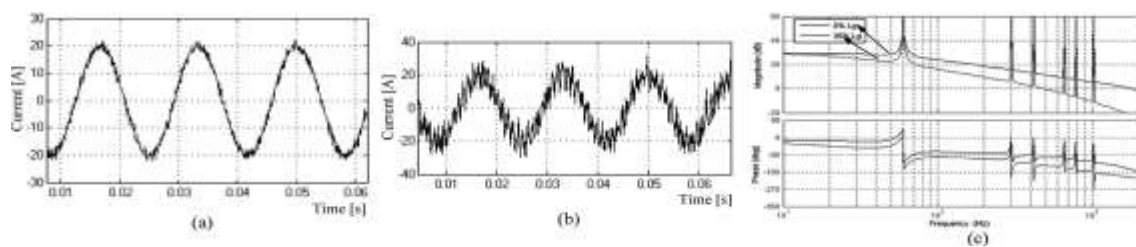


Fig. 6. Performance of the P-HRES controller. (a) Current control performance at nominal parameters. (b)

Current control performance with 35% mismatch in the grid inductance. (c) Frequency characteristics of the P-HRES controller at nominal and uncertain grid inductance. Fig.

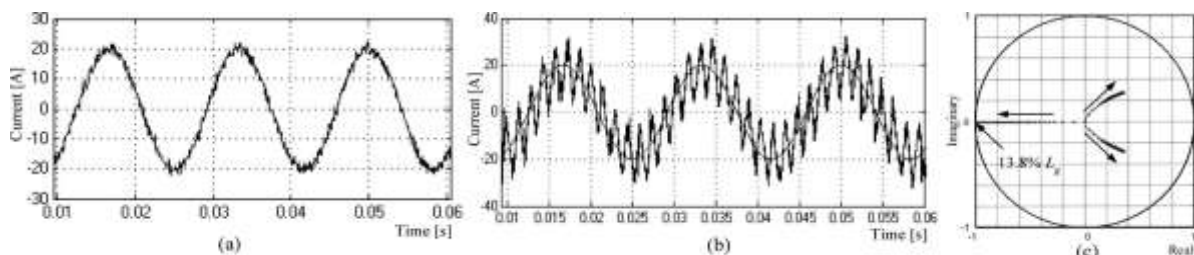
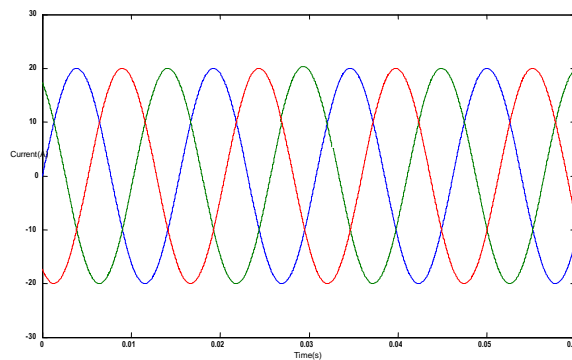


Fig. 7. Performance of the predictive controller (a) Current control performance at nominal parameters. (b)

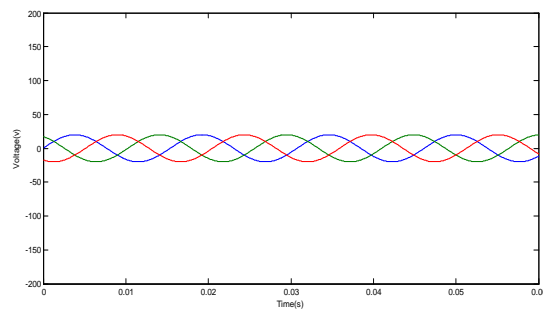
Current control performance with 30% mismatch in the grid inductance. (c) Root locus of the current control dynamics with the grid inductance as a parameter.

Current controller [20] is evaluated. Fig. 7(a) shows the control performance of the predictive controller under nominal system parameters. Fig. 7(b) shows the control performance of the same controller with 30% mismatch of the grid inductance. The robustness of the conventional predictive controller is an issue in grid-connected converter applications. Fig. 7(c) shows the root locus of the current control dynamics with predictive control and with the grid inductance as a parameter. The dominant pole becomes marginally stable with approximately 14% mismatch in the grid inductance. The instability of the current control loop at parameter variation along with the saturation effect of the current control loop and the modulator lead to sustained oscillations in the current response as shown in Fig. 7(b).

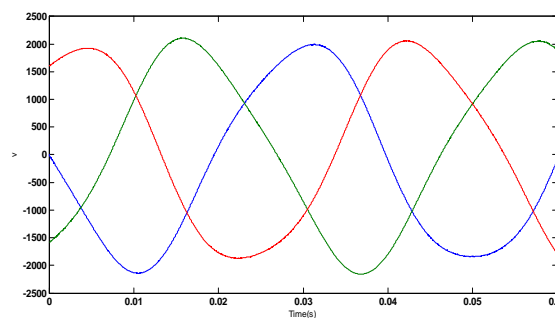
Third, the proposed control scheme is estimated. The controller is evaluated at uncertain grid evaluated. The adaptation gains are selected according to the stability bounds derived in (32)–(34) to yield fast and stable conditions with 60%  $L_g$  and with the aforementioned grid distortion levels. Since the proposed control structure relies on embedding the frequency modes of the grid harmonics and disturbances through the closed-loop current controller, the current controller mainly handles the tracking task whereas the regulation performance is mainly realized through uncertainty estimation and compensation control



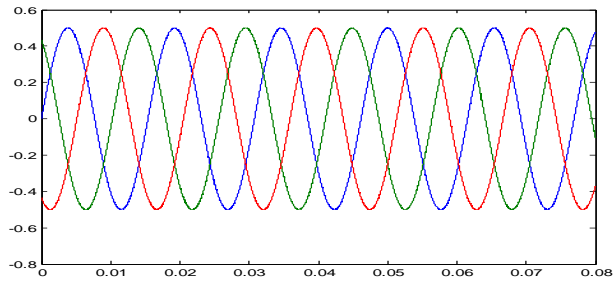
(a)



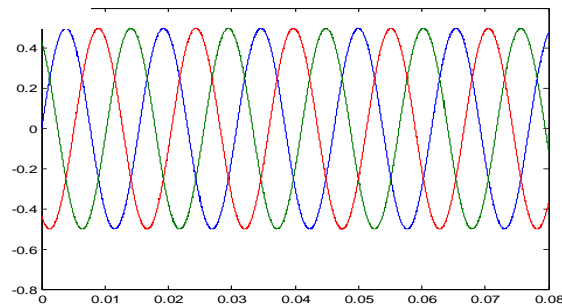
(b)



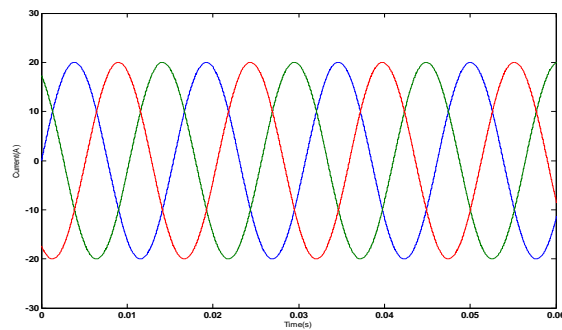
(c)



(d)

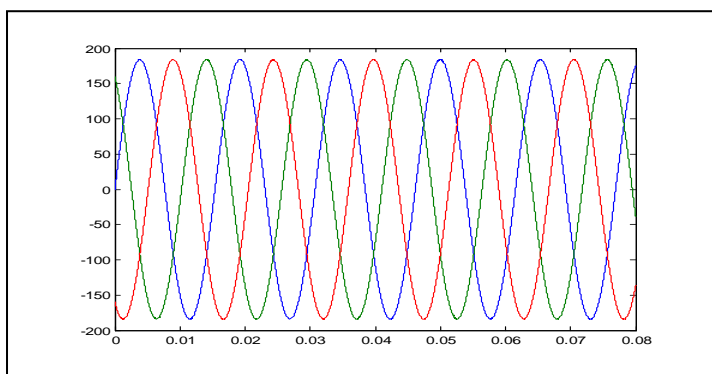


(e)

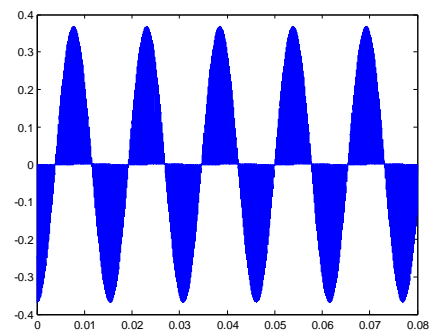


(f)

Fig.8. Dynamic performance of the proposed controller with line-voltage sensorless current control. (a) Controlled current. (b) Active damping voltage.(c) Converter control voltage. (d) Estimated internal model dynamics  $\hat{w}_1$  (e) Estimated internal model dynamics  $\hat{w}_2$ . (f) Estimated internal model dynamics  $\hat{w}_3$ .



(a)



(b)

Fig. 9. (a) Current control performance with Kalman-filter-based estimator. (b) Current tracking error with proposed adaptive internal-model generator and with Kalman-filter-based estimator.

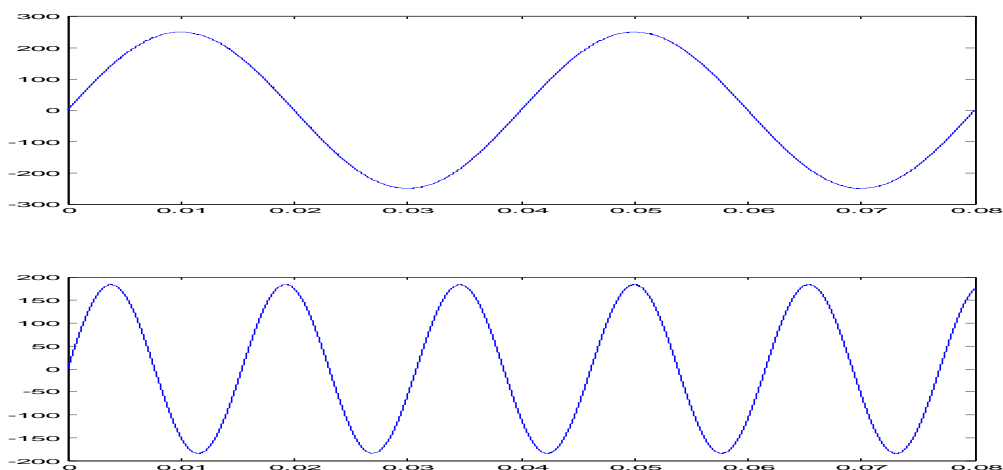
. Fig. 8 shows the control performance of the proposed controller. Fig. 8(a) shows that high power quality current injection, with a THD of 1.95%, is yielded with the proposed current control scheme. This result meets the grid-connection standards; e.g., [26]. The high-quality current injection is the natural result of the high disturbance rejection ability of the proposed current controller.

The converter resonance is well damped due to the active damping control action. Fig. 8(b) shows the injected active damping control voltages using the filtered capacitor current. Fig. 8(c) shows the inverter control voltage. The estimated internal model modes are effectively embedded in the control effort to cancel the effect of grid voltage harmonics, unbalance, and parameter variation. Fig. 8(d), (e), and (f) shows the estimated internal model dynamics  $\hat{w}_1$ ,  $\hat{w}_2$ , and  $\hat{w}_3$ , respectively. The estimated dynamics are generated according to any deviation from the nominal plant model and the actual plant. The estimate  $\hat{w}_2$  closely tracks the grid voltage, which is modeled as an unmeasured external disturbance imposed on the grid-side dynamics. On the other hand, the estimated dynamics  $\hat{w}_1$  and  $\hat{w}_3$  are generated to compensate for the mismatch in system parameters. All estimates closely track actual disturbances with fast convergence properties (with settling time around 1ms and with overshoot less than 10%) as shown in Fig. 8. It can be also noted that the high-bandwidth deadbeat current controller enables such energy shaping control at relatively high frequencies. For further performance comparison, an extended Kalmanfilter-based algorithm [27] has been used to estimate the internal model dynamics in real time. Fig. 9(a) shows the current control performance with the Kalman filter algorithm under grid-voltage harmonics and unbalance. The nature of the Kalman filter-based estimator as a low-pass filter affects the compensation accuracy under periodic and time-varying disturbances, particularly for high-order harmonics. The THD level with the Kalmanfilter-based estimator is 4.8%. On the contrary, the adaptive ability of the proposed adaptive control scheme allows accurate estimation and internal-model generation of such periodic and time-varying disturbances. This feature can be observed in Fig. 9(a), which depicts the current control performance with the proposed control scheme. Fig. 9(b) shows the corresponding current tracking errors with both controllers.

Next, the performance of the overall control scheme with line-voltage sensorless synchronization is evaluated under the aforementioned levels of grid voltage distortion, unbalance and parametric uncertainties. Fig. 10(a) shows the actual grid voltage. Fig. 10(b) shows the estimated internal model dynamics  $\hat{w}_2$ , which closely tracks the grid voltage with fast convergence properties (less than 0.5 ms). Fig. 10(c) shows the estimated fundamental component of the  $\hat{w}_2$ , which converges to the fundamental component of the grid voltage within two cycles. This time delay is mainly related to the response time of the resonant filter. Fig. 10(d) shows the estimated grid angle, which is obtained by the  $dq$ -PLL. Fig. 10(e) shows the injected, which becomes fully synchronized to the fundamental grid voltage within three cycles. Fig. 10 indicates the validity and effectiveness of the proposed voltage-sensorless control and synchronization technique.

## V. Conclusion

A robust control scheme for Ultra capacitor based sensorless current control of grid connected inverter for Power quality improvement high power quality grid connection of  $LCL$ -filtered DG inverters has been presented. The proposed scheme has provided: 1) robust and simple active damping control performance under grid and filter parameter variation; 2) suppression of grid-induced distortion without *a-priori* knowledge of the grid background distortion and unbalance via real-time generation of the frequency modes and disturbances that should be eliminated from the closed-loop current control system; 3) robust deadbeat digital control performance that maximizes the dynamic performance of the converter; and 4) robustness



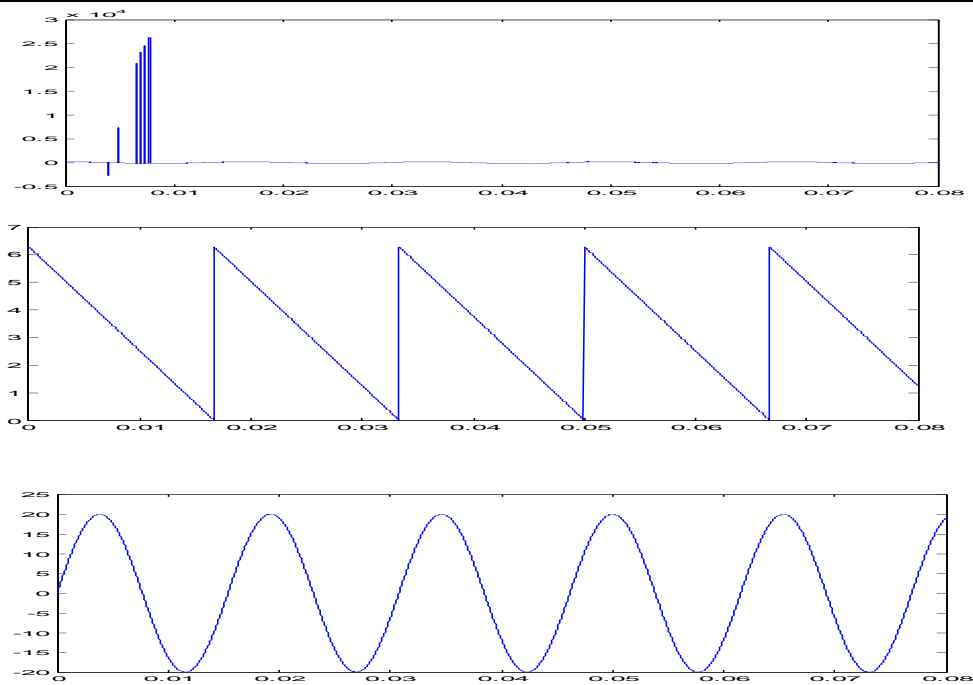


Fig. 10. Dynamic performance of the proposed control scheme with line-voltage sensorless synchronization and current control. (a) Actual grid voltage. (b) Estimated internal model dynamics  $\hat{w}_2$ . (c) Estimated fundamental component of  $\hat{w}_2$ . (d) Estimated grid angle. (e) Controlled current.

Against interaction dynamics between active damping and current tracking controllers. Furthermore, feasible line voltage sensorless current control and grid-synchronization performance has been obtained in the proposed control scheme.

## References

- [1] Yasser Abdel-Rady I. Mohamed, M. A.-Rahman, and R. Seethapathy, "Robust Line-Voltage Sensorless Control and Synchronization of LCL-Filtered Distributed Generation inverters for High Power Quality Grid Connection" *IEEE Trans. Power Electronics*, vol. 27, no. 1, Jan 2012
- [2] The U.S. Department of Energy. (2009). *Smart Grid: An Introduction*.pp.1–48.[Online]. Available: [www.oe.energy.gov/. . /DOE\\_SG\\_Book\\_Single\\_Pages\(1\).pdf](http://www.oe.energy.gov/. . /DOE_SG_Book_Single_Pages(1).pdf).
- [3] E.M.Lightner and S. E.Wideregren, "An orderly transition to a transformed electricity systems," *IEEE Trans. Smart Grid*, vol. 1, no. 1, pp. 3–10, Jun.2010.
- [4] K.Moslehi and R. Kumar, "A reliability perspective of smart grid," *IEEE Trans. Smart Grid*, vol. 1, no. 1, pp. 57–64, Jun. 2010.
- [5] A. Ipakchi and F. Albuyeh, "Grid of the future," in *IEEE Power Energy Mag.*, vol. 7, no. 2, Mar./Apr. 2009, pp. 52–62.
- [6] Y. A.-R. I. Mohamed and A. Radwan, "Hierarchical control system for robust microgrid operation and seamless mode transfer in active distribution systems," *IEEE Trans. Smart Grid*, vol. 2, no. 2, pp. 352–362, Jun.2011.
- [7] J. P. Lopes, C. Moreira, and A. G. Madureira, "Defining control strategies for MicroGrids islanded operation," *IEEE Trans. Power Syst.*, vol. 21, no. 2, pp. 916–924, May 2006.
- [8] Y. A.-R. I. Mohamed and E. F. El-Saadany, "Adaptive decentralized droopcontroller to preserve power-sharing stability of paralleled-inverters in distributed generationmicro-grids," *IEEE Trans. Power Electron.*, vol. 23, no. 6, pp. 2806–2816, Nov. 2008.
- [9] F. Blaabjerg, Z. Chen, and S. B. Kjaer, "Power electronics as efficient interface in dispersed power generation systems," *IEEE Trans. Power Electron.*, vol. 19, no. 5, pp. 1184–1194, Sep. 2004.
- [10] M. Prodanovic and T. C. Green, "Control and filter design of three-phase inverters for high power quality grid connection," *IEEE Trans. Power Electron.*, vol. 18, no. 1, pp. 373–380, Jan. 2003.
- [11] I. J. Gabe, V. F. Montagner, and H. Pinheiro, "Design and implementation of a robust current controller for VSI connected to the grid through an LCL filter," *IEEE Trans. Power Electron.*, vol. 24, no. 6, pp. 1444–1452, Jun. 2009.
- [12] M. Liserre, R. Teodorescu, and F. Blaabjerg, "Stability of photovoltaic and wind turbine grid-connected inverters for a large set of grid impedance values," *IEEE Trans. Power Electron.*, vol. 21, no. 1, pp. 263–272, Jan.2006.
- [13] E. Twinning and D. G. Holmes, "Grid current regulation of a three-phase voltage source inverter with an LCL input filter," *IEEE Trans. Power Electron.*, vol. 18, no. 3, pp. 888–895, May 2003.
- [14] F. Blaabjerg, R. Teodorescu, M. Liserre, and A. V. Timbus, "Overview of control and grid synchronization for distributed power generation systems," *IEEE Trans. Ind. Electron.*, vol. 53, no. 5, pp. 1398–1409, Oct.2006.
- [15] M. Liserre, R. Teodorescu, and F. Blaabjerg, "Multiple harmonics control for three-phase grid converter systems with the use of PI-RES current controller in a rotating frame," *IEEE Trans. Power Electron.*, vol. 21,no. 3, pp. 836–841, May 2006.
- [16] T. C. Y. Wang, Z. Ye, G. Sinha, and X. Yuan, "Output filter design for a grid interconnected three-phase inverter," in *Proc. IEEE Power Electron. Spec. Conf.*, 2003, vol. 2, pp. 779–784.
- [17] M. Liserre, A. Dell'Aquila, and F. Blaabjerg, "Genetic algorithm-based design of the active damping for an LCL-filter three-phase active rectifier," *IEEE Trans. Power Electron.*, vol. 19, no. 1, pp. 76–86, Jan. 2004.
- [18] G. Shen, D. Xu, L. Cao, and X. Zhu, "An improved control strategy for grid-connected voltage source inverter with LCL filter," *IEEE Trans. Power Electron.*, vol. 23, no. 4, pp. 1899–1906, Jul. 2008.

- [19] E. Wu and P.W. Lehn, "Digital current control of a voltage source converter with active damping of LCL resonance," *IEEE Trans. Power Electron.*, vol. 21, no. 5, pp. 1364–1373, Sep. 2006.
- [20] J. Dannehl, F. W. Fuchs, and P. B. Thogersen, "PI state space current control of grid-connected PWM converters with LCL filters," *IEEE Trans. Power Electron.*, vol. 25, no. 9, pp. 2320–2330, Sep. 2010.
- [21] A. Timbus, M. Liserre, R. Teodorescu, P. Rodriguez, and F. Blaabjerg, "Evaluation of current controllers for distributed power generation systems," *IEEE Trans. Power Electron.*, vol. 24, no. 3, pp. 654–664, Mar. 2009.
- [22] A. Papavasiliou, S. Papanthanasios, S. Manias, and G. Demetriadis, "Current control of a voltage source inverter connected to the grid via an LCL filter," in *Proc. IEEE Power Electron. Spec. Conf.*, Orlando, Florida, Jun. 17–21, 2007, pp. 2379–2384.
- [23] M. Jamil, M. Sharkh, S. M. Abusara, and R. J. Boltryk, "Robust repetitive feedback control of a three-phase grid connected inverter," in *Proc. 5<sup>th</sup> IET Int. Conf. Power Electron., Mach. Drives*, 2010, pp. 1–6.
- [24] V. Blasko and V. Kaura, "A novel control to actively damp resonance in input LC filter of a three-phase voltage source converter," *IEEE Trans. Ind. Appl.*, vol. 33, no. 2, pp. 542–550, Mar./Apr. 1997.
- [25] K. J. Astrom and B. Wittenmark, *Adaptive Control*. New York: Addison-Wesley, 1995.
- [26] J. W. Howze and S. P. Bhattacharyya, "Robust tracking, error feedback, and two-degree-of-freedom controllers," *IEEE Trans. Automat. Contr.*, vol. 42, no. 7, pp. 980–983, Jul. 1997.
- [27] *IEEE Standard for Interconnecting Distributed Resources with Electric Power Systems*, IEEE Standard 1547-2003, Jul. 2003.
- [28] R. Dhaouadi, N. Mohan, and L. Norum, "Design and implementation of an extended Kalman filter for the state estimation of a permanent magnet synchronous motor," *IEEE Trans. Power Electron.*, vol. 6, no. 3, pp. 491–491, Jul. 1991.

**Yasser Abdel-Rady I. Mohamed** (M'06–SM'11) was born in Cairo, Egypt, on November 25, 1977. He received the B.Sc. (Hons.) and M.Sc. degrees in electrical engineering from Ain Shams University, Cairo, in 2000 and 2004, respectively, and the Ph.D. degree in electrical engineering from the University of Waterloo, Waterloo, ON, Canada, in 2008. He is currently with the Department of Electrical and Computer Engineering, University of Alberta, Edmonton, Canada, as an Assistant Professor. His research interests include dynamics and controls of power converters, distributed and renewable generation; modeling, analysis and control of smart grids; and electric machines and motor drives. Dr. Mohamed is an Associate Editor of the IEEE TRANSACTIONS ON INDUSTRIAL ELECTRONICS. He is also a Guest Editor of the IEEE TRANSACTIONS ON INDUSTRIAL ELECTRONICS Special Section on "Distributed Generation and Microgrids." His biography is listed in *Marque's who is who in the World*.

**M. A.-Rahman** is currently a Senior Research Engineer in Sustainable Energy Laboratory, National Research Institute, Cairo, Egypt. He is also a Research Engineer with ABB research and Development. His research interests include renewable energy resources, power converters, digital control, and control system implementation.

**R. Seethapathy** (M'76–SM'09) is currently Manager in Distributed Generation, and Advanced Grid Development, Hydro One Networks, Inc., Toronto, ON, Canada. Mr. Seethapathy sits on several T&D/DG committees at the PES/IEEE and CIGRE. He is also a Registered Professional Engineer in the Province of Ontario.